


# Extreme vorticity events in turbulent Rayleigh-Bénard convection from stereoscopic measurements and reservoir computing

Valentina Valori \* and Robert Kräuter*Institute of Thermodynamics and Fluid Mechanics, Technische Universität Ilmenau, D-98684 Ilmenau, Germany*Jörg Schumacher *Institute of Thermodynamics and Fluid Mechanics, Technische Universität Ilmenau, D-98684 Ilmenau, Germany and Tandon School of Engineering, New York University, New York, New York 11201, USA*

(Received 10 December 2021; accepted 10 May 2022; published 3 June 2022)

High-amplitude events of the out-of-plane vorticity component  $\omega_z$  are analyzed by stereoscopic particle image velocimetry (PIV) in the bulk region of turbulent Rayleigh-Bénard convection in air. The Rayleigh numbers  $Ra$  vary from  $1.7 \times 10^4$  to  $5.1 \times 10^5$ . The experimental investigation is connected with a comprehensive statistical analysis of long-term time series of  $\omega_z$  and individual velocity derivatives  $\partial u_i / \partial x_j$ . A statistical convergence for derivative moments up to an order of 6 is demonstrated. Our results are found to agree well with existing high-resolution direct numerical simulation data in the same range of parameters, including the extreme vorticity events that appear in the far exponential tails of the corresponding probability density functions. The transition from Gaussian to non-Gaussian velocity derivative statistics in the bulk of a convection flow is confirmed experimentally. The experimental data are used to train a reservoir computing model, one implementation of a recurrent neural network, to reproduce highly intermittent experimental time series of the vorticity and thus reconstruct extreme out-of-plane vorticity events. After training the model with high-resolution PIV data, the machine learning model is run with sparsely seeded, continually available, and unseen measurement data in the reconstruction phase. The dependence of the reconstruction quality on the sparsity of the partial observations is also documented. Our latter result paves the way to machine-learning-assisted experimental analyses of small-scale turbulence for which time series of missing velocity derivatives can be provided by generative algorithms.

DOI: [10.1103/PhysRevResearch.4.023180](https://doi.org/10.1103/PhysRevResearch.4.023180)

## I. INTRODUCTION

Thermal convection is one of the fundamental mechanisms by which turbulent flows evolve. The temperature dependence of the fluid mass density and the resulting buoyancy forces drive fluid motion that in turn advects the temperature leading to a fully turbulent motion of the fluid [1–4]. The simplest configuration in this specific class of turbulent flows is Rayleigh-Bénard convection (RBC)—a fluid layer of height  $H$  between two parallel rigid plates heated uniformly from below and cooled uniformly from above, such that a constant temperature difference  $\Delta T = T_{\text{bot}} - T_{\text{top}} > 0$  is sustained across the layer. Experimentally, RBC can be realized in a horizontally extended closed cylindrical or cuboid cell with thermally insulated sidewalls. In the past two decades, a larger number of direct numerical simulations (DNSs) of this configuration investigated various aspects of large-scale struc-

ture formation, longer-term dynamics, and the dependencies on Rayleigh and Prandtl numbers,  $Ra$  and  $Pr$ , as well as on the aspect ratio  $\Gamma$  of the cells in detail [5–17]. The number of studies of RBC in air at a Prandtl number of  $Pr = 0.7$  by means of controlled laboratory experiments is much smaller; see, e.g., Refs. [18–22] for investigations in large-aspect-ratio setups. The three dimensionless control parameters of RBC experiments are defined as follows,

$$Ra = \frac{g\alpha\Delta TH^3}{\nu\kappa}, \quad Pr = \frac{\nu}{\kappa}, \quad \Gamma = \frac{L}{H}. \quad (1)$$

Here,  $g$  is the acceleration due to gravity,  $\alpha$  is the thermal expansion coefficient,  $\nu$  is the kinematic viscosity,  $\kappa$  is the thermal diffusivity, and  $L$  is the horizontal lengthscale.

The dynamics and structure of the boundary layers of the velocity and temperature fields at the top and bottom of an RBC layer are essential for the amount of heat that can be carried from the bottom to the top in this configuration. In Ref. [23], a dynamical connection between this dynamics and the small-scale intermittent motion in the bulk, in particular the formation of high-amplitude dissipation events, was established. Thermal and kinetic energy dissipation fields probe the magnitude of gradients of the temperature and velocity fields, respectively. Their amplitudes are known to be largest at the smallest scales [24–27]. In detail, it was shown in [23] how

\*valentina.valori@tu-ilmenau.de

the formation of coherent plumes at the top and bottom and their subsequent collision or passing create large temperature gradients in the bulk that cause the formation of localized shear layers; see also Ref. [28] for a closed cylindrical cell at unit aspect ratio. These studies set one motivation for the present work.

In the present work, we want to study the velocity derivatives in the bulk of an RBC configuration experimentally by means of stereoscopic particle image velocimetry (SPIV) in the midplane of the horizontal cell. This allows us to obtain all three velocity components  $u_i(\mathbf{x}, t)$  in a horizontal measurement region  $A = 2.9H \times 2.2H$  and thus seven out of the nine components of the velocity gradient tensor field  $M_{ij}(\mathbf{x}, t) = \partial u_i / \partial x_j$ . These are the in-plane components  $\partial u_i / \partial x_j$  with  $i = 1, 2, 3$  and  $j = 1, 2$  and  $\partial u_3 / \partial x_3 = -(\partial u_1 / \partial x_1 + \partial u_2 / \partial x_2)$  via the incompressibility condition of the flow. Thus the out-of-plane component of the vorticity field  $\omega_3 = \partial u_2 / \partial x_1 - \partial u_1 / \partial x_2$  can be obtained, and we have access to highly intermittent derivative fields in the bulk of the turbulent convection layer. We analyze the statistics of these seven derivatives and probe their statistical convergence. Furthermore, the resulting probability density functions (PDFs) are found to agree with those of existing high-resolution DNS data from Ref. [23] in a similar setup and the same parameter range.

The SPIV snapshot series contain a few extreme events in the form of intense vortex cores that sweep across the measurement plane  $A$ . In the second part of this work, we analyze their temporal growth and explore the capability of recurrent neural network (RNN) architectures to reconstruct high-amplitude or extreme events of the out-of-plane vorticity component [29]. More specifically, we therefore apply the reservoir computing model (RCM) [30,31], which has been shown to successfully predict the time evolution of nonlinear dynamical and fluid mechanical systems. Examples for the latter case are the Kuramoto-Sivashinsky equation [32–34], low-dimensional Galerkin models of wall-bounded shear flows [35,36], the two-dimensional Kolmogorov flow [37], or two-dimensional RBC configurations without and with phase changes [38,39]. It should also be mentioned that other methods for the temporal predictions of complex dynamics are available that do not rely on neural network approaches, such as the Koopman framework with nonlinear forcing [36].

We show that an RCM with continually available sparse data is able to reconstruct high-amplitude or extreme out-of-plane vorticity events, which can be quantified by a squared vorticity integrated over  $A$  (see Ref. [40] for a recent review). In other words, the present machine-learning algorithm thus operates in an open-loop scenario after the training phase and continues to use previously unseen sparse data. The prescribed data amount to a percentage of the full PIV resolution, which varies between 1.9% and 11%.

The outline of the manuscript is as follows. In Secs. II A–II C, details on the experiment and machine-learning algorithm are provided. Section III A discusses the results with respect to the vorticity and velocity derivative statistics. Furthermore, we investigate the dynamics of a particular high-vorticity event tracked in the experiment in Sec. III B. Section III C finally provides the results of the application of the RNN to reconstruct the time evolution and the non-Gaussian PDFs with the extended tails. We conclude the work

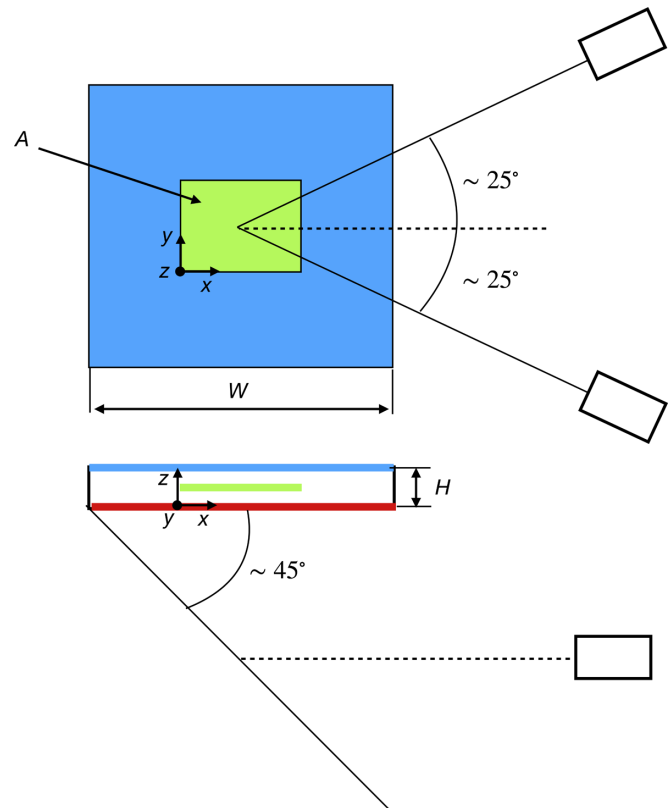


FIG. 1. Relative positions of cameras (shown as rectangles), RB cell, and measurement section from the top and side view. The heated bottom plate of the RB cell and the cooled top plate are indicated by a red and a blue line, respectively. The measurement section  $A$  is represented in green.  $W$  and  $H$  are the horizontal and the vertical dimensions of the cell, respectively.

with a summary and an outlook in Sec. IV. For convenience, we will also switch from the notation  $u_1, u_2, u_3$ , and  $\omega_3$  for velocity and vorticity field components to  $u_x, u_y, u_z$ , and  $\omega_z$  in the following sections with coordinate  $z$  parallel to the inferred temperature gradient between top and bottom.

## II. METHODS

### A. Rayleigh-Bénard convection cell for pressurized air

The experimental setup is a large-aspect-ratio Rayleigh-Bénard convection (RBC) cell of size  $W \times W \times H$ , where the horizontal dimension  $W$  is ten times larger than the vertical distance between the two plates  $H$ , the latter being 3 cm (see Fig. 1). The aspect ratio of the cell is therefore  $\Gamma = 10$ . The bottom plate of the cell is made of two glass plates coated on one side with a thin layer of indium tin oxide. It has the important characteristic of being transparent and at the same time uniformly heatable by the Joule effect. The latter arises from the electrical current that goes through the oxide layer (for further details, see [21]). Each plate has a measured light transmission coefficient of about 68% [21]. This coating was manufactured at the Fraunhofer Institute for Organic Electronics in Dresden (Germany). The top plate of the RBC cell is made of aluminum with an internal cooling circuit where water flows at a controlled temperature fed by a thermo-

stat. The side walls are made of 4-mm-thick polycarbonate, which allows optical access for the laser light. The surface temperatures at both horizontal walls were measured by four thermoresistances PT100 (class B) for each plate, which were located 20 mm from the side walls.

The RBC cell is inserted in the high-pressure facility, i.e., the Scaled Convective Airflow Laboratory Experiment (SCALEX). This facility consists of a high-pressure vessel with 35 observation windows, allowing for optical access from the outside. The pressure within the vessel can be regulated from 10–100 mbars to 8 bars in steps of about 100 mbars. The working pressure was measured with a Cerabar PMC131 sensor from Endress + Hauser AG. Further details on the device are summarized, e.g., in Ref. [21].

### B. Particle image velocimetry measurements

Stereoscopic particle image velocimetry experiments are performed in a horizontal layer at midheight between the top and bottom plate of the cell. The position of the measurement plane is shown in green in Fig. 1. The measurement region covers a horizontal area of  $A \approx 2.9H \times 2.2H$ . To conduct SPIV measurements in a horizontal plane within the cell, two cameras are located below the cell, which take images through the transparent bottom plate. A mirror is placed in the optical path as represented in Fig. 1. A stereo angle of about  $50^\circ$  is used. The cameras are sCMOS from LaVision GmbH with a digital resolution of  $2560 \times 2160$  pixels and a pixel pitch of  $6.5 \mu\text{m}$ . Therefore, the image magnification factor is  $M \sim 0.2$ . The cameras have particularly thin connector cables made of optical fibers that allow them to be placed inside the high-pressure vessel. These cables are inserted into feed-through systems for high pressure from Spectite<sup>®</sup> that are built in a flange of the vessel. The images are recorded at a frame rate of 10 Hz with an interframe time of 7 or 10 ms depending on the strength of the convective flow (or Rayleigh number Ra) studied. Each camera is equipped with a Zeiss Milvus 2/100M objective lens under the Scheimpflug condition. The focal length of the lenses is 100 mm, and the aperture stop used is 5.6 and 8 for the camera in forward and backward scattering, respectively. Both cameras and lenses are placed inside the vessel at a working pressure of up to 4.5 bars. The laser light sheet was created with a double pulse laser (Quantel Q-smart Twins 850) with a pulse energy of about 175 mJ for a 2-mm-thick light sheet. A spherical and a cylindrical lens were used to generate the light sheet.

The depth of field of the measurements  $\delta_z$  is given by

$$\delta_z = 4 \left( 1 + \frac{1}{M} \right)^2 f_{\#}^2 \lambda, \quad (2)$$

where  $\lambda$  is the wavelength of the laser. Here,  $\lambda = 532 \text{ nm}$  for the green laser is used. For the camera in forward scattering with the smallest  $f$ -stop  $f_{\#}$ , the depth is  $\delta_z = 2.4 \text{ mm}$ , which is larger than the laser sheet thickness and therefore ensures good focusing conditions of the illuminated particles. The geometrical calibration is made on the measurement plane with the three-dimensional target 204-15 from LaVision, where the distance between two dots is 15 mm, and the dot diameter and level separation are both 3 mm. Additionally, a stereoscopic self-calibration [41] is made and iteratively repeated with

TABLE I. Summary of the experimental conditions used in the convection measurements. The first column reports the Rayleigh numbers, the second and third columns display the values of the top ( $T_{\text{top}}$ ) and bottom ( $T_{\text{bot}}$ ) temperature, respectively, the fourth column shows the temperature difference between the bottom and the top walls ( $\Delta T$ ), and the fifth column shows the working pressure. The sixth and seventh columns are for the characteristic free-fall velocity and free-fall time of the flow, respectively.

Ra	$T_{\text{top}}$ (°C)	$T_{\text{bot}}$ (°C)	$\Delta T$	$p$ (bars)	$U_{\text{ff}}$ (mm/s)	$T_{\text{ff}}$ (s)
$1.7 \times 10^4$	22.3	28.9	6.6	1	80.7	0.4
$2.1 \times 10^4$	21.2	29.2	8	1	80.7	0.4
$1.1 \times 10^5$	21.2	28.5	7.3	2.47	85	0.35
$2.9 \times 10^5$	22.9	28.4	5.5	4.5	74.3	0.4
$5.1 \times 10^5$	20.1	29.9	9.8	4.5	98.8	0.3

final mean residual displacement below 1 pixel. This final value cannot be further reduced using images of a thermal convection flow because of the presence of optical distortions due to variations in the mass density of the imaging medium [42–44].

The seeding in the PIV measurements is established by droplets of di(2ethylhexyl)sebacate (DEHS) with an average diameter of  $0.9 \mu\text{m}$  generated by a vaporizer from PIVTECH GmbH that is placed inside the pressure vessel. The characteristic velocity of the flow is estimated as the free-fall velocity  $U_{\text{ff}} = \sqrt{\alpha g \Delta T H}$ ; see also Table I for the values of  $U_{\text{ff}}$  and  $\Delta T$ . The sedimentation velocity of the particles of diameter  $d_p$ , which are used here as tracers, is given by

$$u_s = \frac{d_p^2 (\rho_p - \rho_f)}{18 \mu g}, \quad (3)$$

where  $\rho_f$  and  $\mu = \rho_f \nu$  are, respectively, the density and the dynamic viscosity of the fluid at the mean temperature and pressure of the cell, and  $\rho_p$  is the mass density of the particles. The sedimentation velocity of the particles used is negligible as can be seen by the ratio  $u_s/U_{\text{ff}}$ , which is about  $4 \times 10^{-6}$  or smaller for all flow conditions studied here. The particles faithfully follow the flow as indicated by the values of the dimensionless Stokes number, St, defined as the ratio between the characteristic response time of a suspended particle and the characteristic time of the flow,

$$\text{St} = \frac{d_p \rho_p U_{\text{ff}}}{18 \mu g}. \quad (4)$$

The values of the Stokes number in the present study are always  $\text{St} < 10^{-2}$ , as requested for good tracer particles [45,46].

The PIV images are acquired and processed with the software DaVis 10 from LaVision. The only preprocessing that is applied to the raw images is a time-averaged image subtraction in order to reduce the noise. A two-passes cross-correlation algorithm with decreasing interrogation window size is used. The size of the final pass is  $128 \times 128$  pixels for all measurements except for the largest Rayleigh number, where the size is  $96 \times 96$ , which leads to a spatial resolution of about 4 and 3.5 mm, respectively (see Table II). Here, we also list the Kolmogorov length  $\eta_K$  of the DNS (at the comparable

TABLE II. Kolmogorov lengthscale from the direct numerical simulations (DNSs) and spatial resolution of the PIV measurements computed without overlap for each of the five Rayleigh numbers studied. The simulations were conducted in a domain of  $\Gamma = 8$  with periodic boundary conditions at the sidewalls at  $\text{Pr} = 1$  by a spectral element method; see Ref. [23] for details.

$\text{Ra}^{\text{DNS}}$	$\eta_K$ (mm)	$\text{Ra}^{\text{PIV}}$	$\Delta x^{\text{PIV}}$ (mm)
$1.5 \times 10^4$	2.4	$1.7 \times 10^4$	4
$2 \times 10^4$	2.2	$2.1 \times 10^4$	4
$1 \times 10^5$	1.3	$1.1 \times 10^5$	4
$2 \times 10^5$	1.0	$2.9 \times 10^5$	4
$5 \times 10^5$	0.7	$5.1 \times 10^5$	3.5

Rayleigh numbers), which are given in dimensionless units by

$$\eta_K = \left( \frac{\text{Pr}}{\text{Ra}} \right)^{3/8} \langle \epsilon \rangle_{V,t}^{-1/4}, \quad (5)$$

where  $\langle \epsilon \rangle_{V,t}$  is the combined volume-time average of the kinetic energy dissipation rate field [25]. This value is multiplied with the actual cell height  $H$  to get a length in physical units as shown in the table.

The values of Rayleigh numbers of the experiments range from  $\text{Ra} = 1.7 \times 10^4$  to  $5.1 \times 10^5$  and are listed in Table I. The working fluid is air with  $\text{Pr} = 0.7$  for all cases. Rayleigh numbers  $\text{Ra} \geq 1.1 \times 10^5$  are obtained by putting the vessel under pressure. In Table I, the corresponding values of the working pressure of each experiment are shown together with the values of the temperatures at the bottom ( $T_{\text{bot}}$ ) and top ( $T_{\text{top}}$ ) walls of the cell in addition to the resulting difference  $\Delta T$ . The last two columns of the table indicate the characteristic free-fall velocity  $U_{\text{ff}}$  and resulting free-fall time  $T_{\text{ff}} = H/U_{\text{ff}}$  of the flow. Values of the fluid properties are taken from the NIST RefProp database version 9.1 [47].

The major source of uncertainties in this experimental study is due to density variations within the fluid, which are caused by local temperature gradients. The relative density differences between the bottom and the top of the cell were up to 3.4% for the largest Rayleigh number studied. They caused errors in the determination of the three-dimensional particle position and velocity, mostly due to instantaneous and local changes in the magnification factor, which is connected to the motion of thermal plumes [42,43,48]. A global *a posteriori* estimation of the relative velocity uncertainty of the SPIV measurements based on the correlation statistics method [49] gives an upper bound of 0.6% for the experiment at the smallest Rayleigh number and of 2.5% for that at the largest.

### C. Reservoir computing model

In the following, we briefly review the reservoir computing model (RCM) [30]. Our algorithm is a supervised machine-learning algorithm that is run as a single validation split. This includes (i) training, (ii) validation, and (iii) test phases. The PIV data are correspondingly split into three subsets. Other more complex scenarios, such as  $k$ -fold cross validations, are possible and have been discussed only recently for RCMs in Ref. [50].

The reservoir is a random, recurrently and sparsely connected network. The model consists of the input layer, the reservoir, and the output layer, as shown in Fig. 2(a). The input layer takes the training data in the form of discrete time series  $\mathbf{\Omega}^{\text{in}}(t) = [\omega_z^1(t), \dots, \omega_z^{N_{\text{in}}}(t)]$  with  $N_{\text{in}}$  the number of selected grid points of the PIV measurement region  $A$ ; see the red squares in Fig. 2(b). Vorticity data are converted at each instant into a reservoir state vector  $\mathbf{r}(t) \in \mathbb{R}^N$  with a number of reservoir nodes  $N \gg N_{\text{in}}$ . This is done by a random weight matrix  $W^{\text{in}} \in \mathbb{R}^{N \times N_{\text{in}}}$  which is determined at the beginning of the training and left unchanged,

$$\mathbf{r}(t) = W^{\text{in}} \mathbf{\Omega}^{\text{in}}(t). \quad (6)$$

The reservoir is described by a symmetric adjacency matrix  $W^r \in \mathbb{R}^{N \times N}$ , also determined initially as a random matrix and left unchanged. Typically, an ensemble of different random realizations of the reservoir matrix is considered in the training process. Two important parameters of  $W^r$  are the reservoir density  $D$  of active nodes and the spectral radius  $\rho(W^r)$ , which is set by the largest absolute value of the eigenvalues. The reservoir nodes are updated by a simple nonlinear dynamical system. The discrete time evolution is given by

$$\begin{aligned} \mathbf{r}(t + \Delta t) &= (1 - \alpha) \mathbf{r}(t) \\ &+ \alpha \tanh[W^r \mathbf{r}(t) + W^{\text{in}} \mathbf{\Omega}^{\text{in}}(t)], \end{aligned} \quad (7)$$

where nonlinearity enters in the form of an activation function, here by a hyperbolic tangent. The leakage rate is  $0 < \alpha < 1$  and the spectral radius of the reservoir is typically taken  $\rho(W^r) \lesssim 1$ . The final of the three building blocks of the RCM is the output weight matrix  $W^{\text{out}} \in \mathbb{R}^{N_{\text{PIV}} \times N}$  which maps the updated reservoir vector back to the vorticity field and is not random,

$$\hat{\mathbf{\Omega}}^{\text{out}}(t + \Delta t) = W^{\text{out}} \mathbf{r}(t + \Delta t). \quad (8)$$

Here,  $N_{\text{PIV}}$  is the number of all grid points of the PIV measurement region  $A$ . The iteration of (7) is repeated for all the snapshots of the PIV training data, and the sequence of corresponding reservoir states is saved. In contrast to most other neural networks, the training of the RCM is performed with respect to the output layer only. The optimized output weight matrix,  $W^{\text{out}*}$ , is obtained by a minimization of a regularized quadratic cost function  $C$ . The regularization term is added to  $C$  to tackle the overfitting problem [29]. This cost function is given by

$$\begin{aligned} C[W^{\text{out}}] &= \sum_{k=1}^{N_{\text{train}}} |W^{\text{out}} \mathbf{r}(k\Delta t) - \mathbf{\Omega}(k\Delta t)|^2 \\ &+ \gamma \text{Tr}(W^{\text{out}} W^{\text{out}T}), \end{aligned} \quad (9)$$

where  $\mathbf{\Omega}(k\Delta t)$  is the ground truth, i.e., the PIV data. To summarize, the hyperparameters of the RCM training process are the number of nodes  $N$ , the reservoir density  $D$ , the spectral radius  $\rho(W^r)$ , the leakage rate  $\alpha$ , and the ridge regression parameter  $\gamma > 0$  of the regularization term of the cost function  $C$ . Here, we will leave  $D = 0.2$ . The remaining hyperparameters span a four-dimensional space and have to be tuned. In the *training phase*, we take 100 different quadruples  $\{N, \rho(W^r), \alpha, \gamma\}$  randomly from prescribed ranges and run the RCM for each quadruple and 10 different initial random

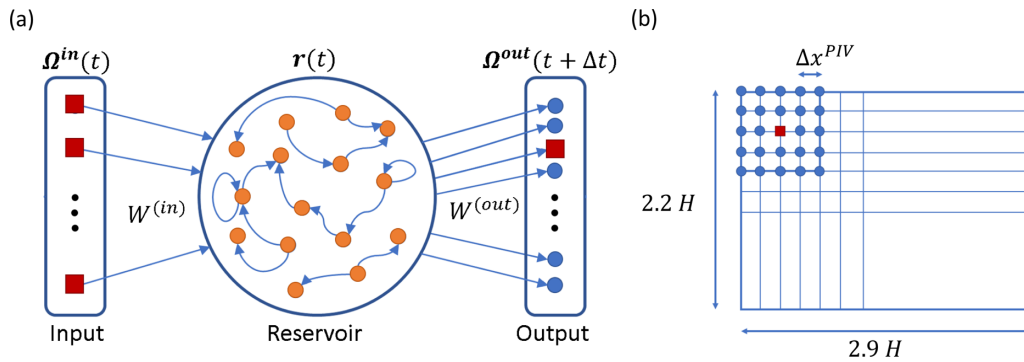


FIG. 2. Sketch of the reservoir computing model (RCM) and arrangement of continually available data during the prediction phase of the machine-learning algorithm, indicated as red filled squares. (a) The three building blocks of the RCM are the input layer, the reservoir (a random network of neurons), and the output layer. (b) Sketch of a part of the data grid  $A$  of  $N_{PIV}$  points obtained in the stereoscopic particle image velocimetry (PIV) measurement. This figure illustrates the  $5 \times 5$  scenario: one data point with continually available experimental vorticity data (red filled square) is surrounded by 24 grid points (blue filled circles) for which the trained RCM predicts the time evolution of the vorticity component autonomously. Thus 3.5% of the full PIV resolution is available in the reconstruction phase and  $N_{in} \ll N_{PIV}$ . The whole measurement area  $A$  is covered sparsely with continually available measurements in this way. The uniform PIV resolution is also indicated.

seeds of the reservoir to optimize  $W^{out}$  for each of the  $10^3$  training runs. The subsequent *validation phase* selects the optimal hyperparameter set as the one that gives the minimal mean-squared error (MSE). This leads to the optimal output matrix  $W^{out*}$  for the optimal quadruple  $\{N^*, \rho(W^r)^*, \alpha^*, \gamma^*\}$ .

In the final *reconstruction phase*, the RCM reconstructs the vertical vorticity component field in the measurement region that can be compared with original unseen test data. The RCM generates synthetic time series of the intermittent vorticity component at all grid points of the measurement region  $A$  from sparse continuously provided data at a subset of grid points of  $A$ . The RCM is run in a mode that is sometimes referred to as an open-loop scenario or one-step prediction [50] since the reservoir output is not used as an input for the subsequent step.

### III. RESULTS

#### A. Velocity derivative statistics

The long total measurement acquisition time of  $2500 T_{ff}$  allows a good convergence of the statistics as displayed in Fig. 3. In these plots, we report results of the out-of-plane vorticity and selected individual velocity derivative components, all normalized by their corresponding root-mean-square (rms) values. We therefore define

$$\chi := \frac{\omega_z}{\sqrt{\langle \omega_z^2 \rangle_{A,t}}} \quad \text{or} \quad \chi := \frac{\partial u_i / \partial x_j}{\sqrt{\langle (\partial u_i / \partial x_j)^2 \rangle_{A,t}}}, \quad (10)$$

with  $i, j = 1, 2, 3$ . The denominators in both equations are the root-mean-square (rms) values of the corresponding quantities. The statistical convergence of the  $n$ th-order normalized moment follows from plots of  $\chi^n p(\chi)$  versus  $\chi$ . The area below these curves corresponds then to the  $n$ th-order moment  $M_n$ , which is given by

$$M_n(\chi) := \int_{-\infty}^{\infty} \chi^n p(\chi) d\chi. \quad (11)$$

These moments can be evaluated in a discretized approximation of this integral. The statistical convergence of moments

$M_2, M_4$ , and  $M_6$  is shown in Fig. 3 for the two largest experiment Rayleigh numbers  $Ra = 2.9 \times 10^5$  and  $5.1 \times 10^5$ . A converged velocity derivative statistics implies that the tails for the largest  $\chi$ -values tend to decay to zero, which seems to be the case for the shown components. Note that the y-axes are displayed in logarithmic units in the figure. We have also verified that the two velocity gradient tensor components, which are not shown in the figure, satisfy the statistical convergence criteria as well. It can be confirmed that the PIV measurements obtain sufficiently well-resolved velocity gradients in the range of accessible Rayleigh numbers.

Figure 4 reports a direct comparison between the PDFs of five components of the velocity gradient tensor  $A_{ij}$  and the out-of-plane vorticity component  $\omega_z$  from the SPIV measurements and the DNS data from [23]. One can see that the experimental results are in very good agreement with the simulation data all the way to the far tails. Again, the PDFs of the two missing components,  $\partial u_z / \partial x$  and  $\partial u_z / \partial y$ , are qualitatively and quantitatively similar to the shown data.

The PDFs of the out-of-plane vorticity of the SPIV of all series as displayed in Table II are shown in Fig. 5. One can observe that the tails of the PDFs become wider as the Rayleigh number grows, which is an indication of a transition from Gaussian to non-Gaussian intermittent velocity derivative statistics as discussed for RBC in Refs. [23,51,52]. We can thus conclude that this transition is also detectable in the bulk of controlled laboratory experiments at moderate Rayleigh numbers. This allows us to run long-term measurements of velocity derivative statistics, which is challenging in simulations where the numerical effort grows with  $\Gamma^2$ .

#### B. Extreme event of out-of-plane vorticity

An example of an extreme event of  $\omega_z$  from PIV measurements at Rayleigh number  $Ra = 5.1 \times 10^5$  is shown in Fig. 6. We consider an event extreme whenever the vorticity magnitude exceeds  $10\omega_{z,rms}$ . In the time interval at the highest Rayleigh number, we were able to record two of these events.

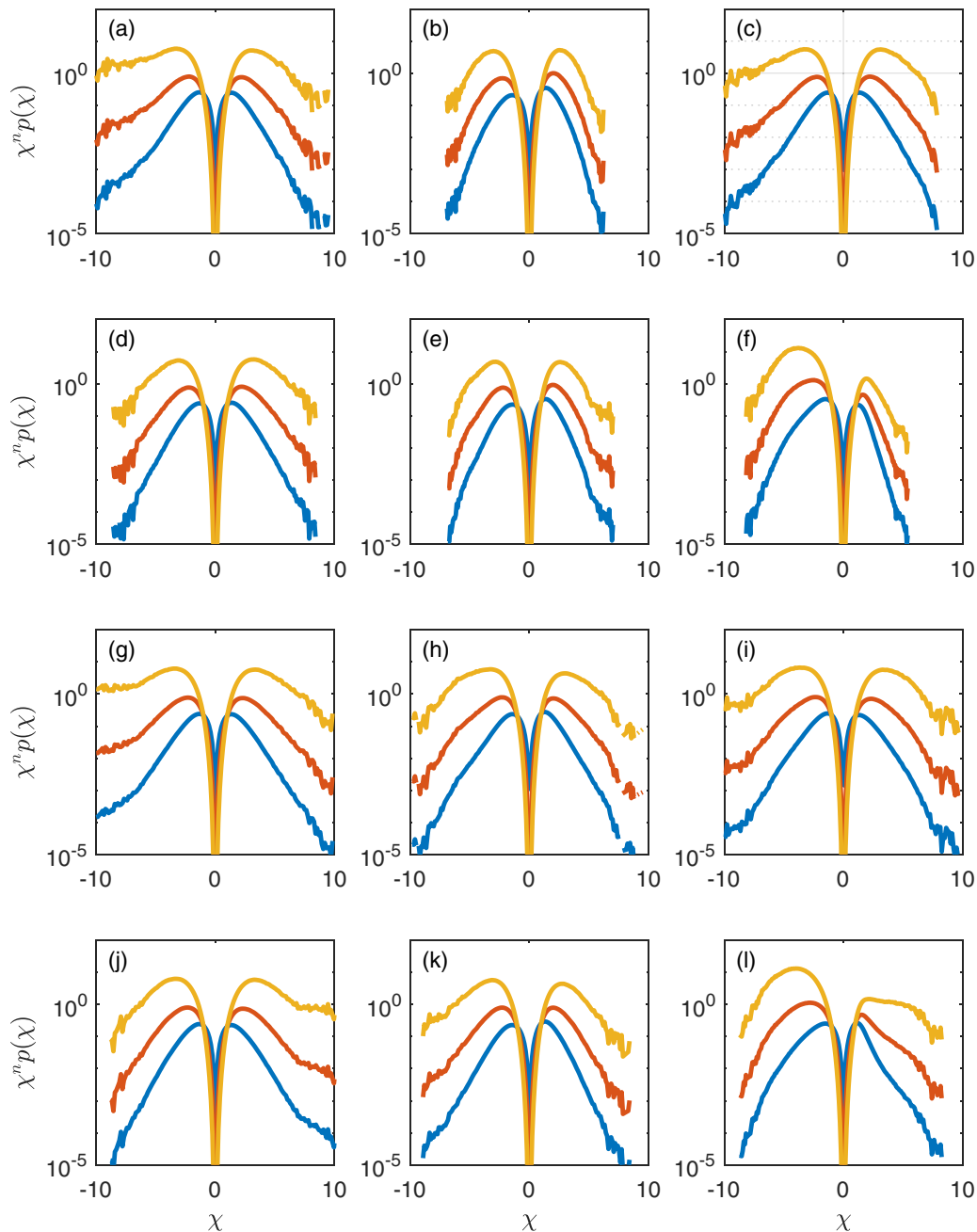


FIG. 3. Statistical convergence of the higher-order velocity derivative statistics in the experiments. The vorticity component  $\omega_z$  (a),(g) and the derivatives  $\partial u_x/\partial x$  (b),(h),  $\partial u_y/\partial x$  (c),(i),  $\partial u_x/\partial y$  (d),(j),  $\partial u_y/\partial y$  (e),(k), as well as  $\partial u_z/\partial z$  (f),(l) are shown. All derivatives are normalized by their corresponding root-mean-square values. The moment order  $n$  is indicated in the legend above the panels. Panels (a)–(f) are for  $Ra = 2.9 \times 10^5$ , while panels (g)–(l) are for  $Ra = 5.1 \times 10^5$ .

It can be expected that their frequency and excess magnitude increase when the Rayleigh number grows. This point is left as future work. Panel (a) of the figure shows a prominent vortex core on the right-hand side of  $A$ . This vortex is the result of a horizontal shear in combination with an upward motion through the observation plane. From the corresponding velocity field, whose components are represented in panels (b)–(d) of this figure, one can suspect that a plume collision is responsible for the generation of the extreme vorticity event, as was observed so far only in DNS data records [23]. Lu and Doering [53] showed that the temporal growth of the

enstrophy, which is given by

$$\bar{E}(t) = \int_V \omega_i^2 dV \quad \text{with} \quad \omega_i(\mathbf{x}, t) = \varepsilon_{ijk} \frac{\partial u_k(\mathbf{x}, t)}{\partial x_j}, \quad (12)$$

in homogeneous isotropic turbulence in a triply periodic box of volume  $V$ , is rigorously bounded by

$$\frac{d\bar{E}(t)}{dt} \leq \frac{27c^3}{16\nu^3} \bar{E}(t)^3, \quad (13)$$

with  $c = \sqrt{2/\pi}$ . It was found that axially symmetric, colliding vortex rings maximize the enstrophy growth, and that

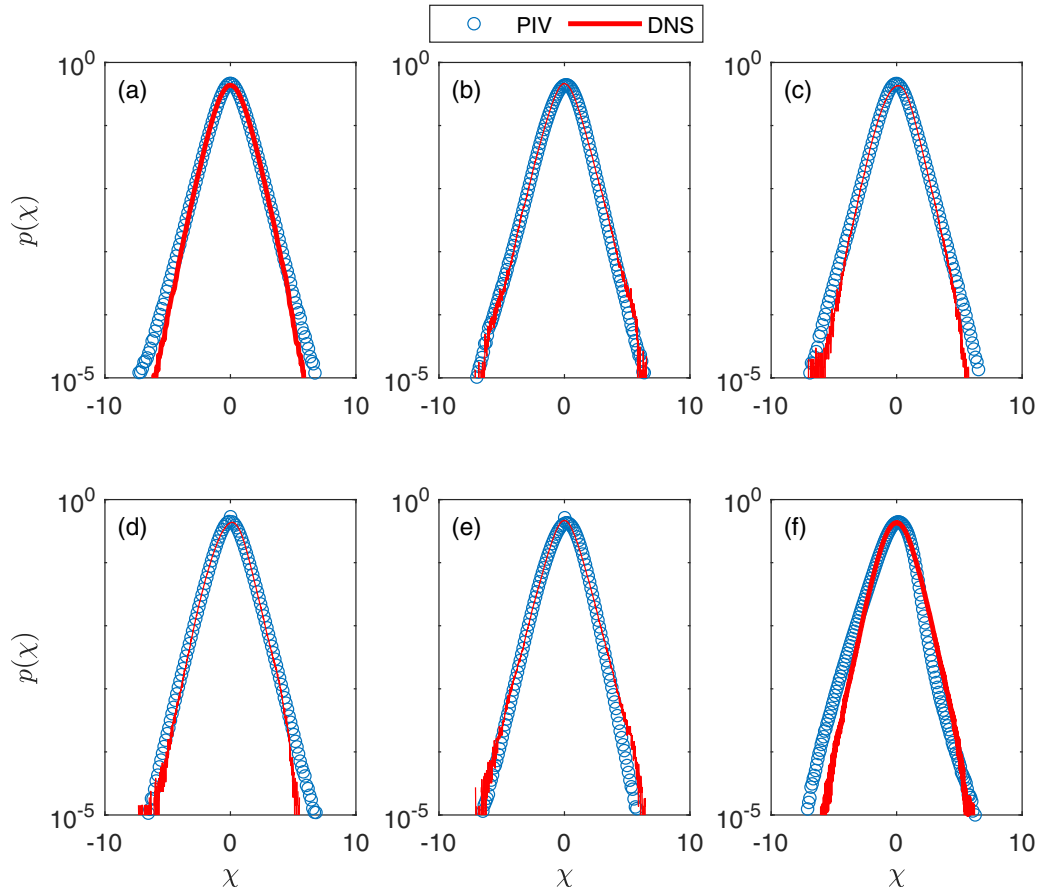


FIG. 4. Comparison of the probability density function of out-of-plane vorticity  $\omega_z$  (a) and the five partial derivatives, which are  $\partial u_x/\partial x$  in (b),  $\partial u_y/\partial x$  in (c),  $\partial u_x/\partial y$  in (d),  $\partial u_y/\partial y$  in (e), and  $\partial u_z/\partial z$  in (f). The PIV experiments are at  $Ra = 5.1 \times 10^5$ , while the DNS is at  $Ra = 5 \times 10^5$ . All quantities are normalized by their corresponding root-mean-square values.

interacting Burgers vortices cause a growth  $d\bar{E}/dt \sim \bar{E}(t)^{7/4}$ . Even though we cannot expect that the same bound holds for a turbulent convection flow, we can probe the growth of the

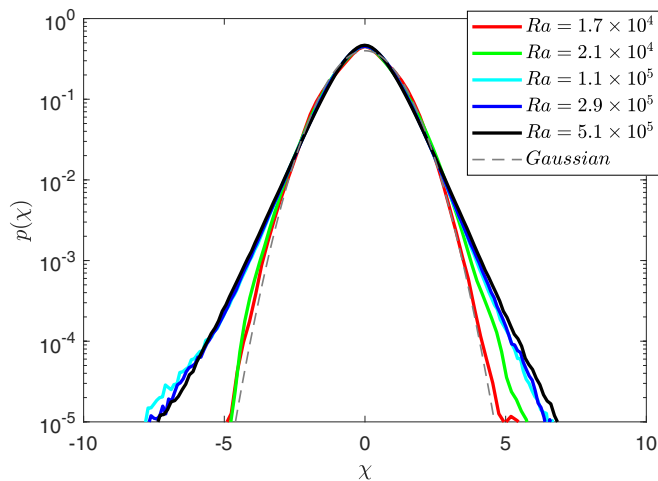


FIG. 5. Probability density functions of the out-of-plane vorticity field component obtained from different stereoscopic particle image velocimetry measurements for the Rayleigh numbers which are indicated in the legend. The gray dashed line displays the Gaussian case for reference.

out-of-plane squared vorticity in the measurement region  $A$ . In Fig. 7, we therefore plot the temporal growth of the vorticity component,  $d\omega_z^2/dt$ , versus the squared vorticity,  $\omega_z^2$ , as a scatter plot for all grid points that are centered around  $\mathbf{x}_* \in A$ , the point where  $\omega_z^2$  yields an extreme event at time  $t = t_*$ . In both panels, the time series (which extend over  $10^4$  data points) are plotted for  $5 \times 5$  grid points. The data right before  $t = t_*$  are replotted in blue in both panels. In addition, the growth laws with the exponents 3 and 7/4 are also indicated by solid lines. It is seen that for the highest-amplitude extreme event, the growth to the maximum is close to the 7/4-scaling, which suggests that a vortex stretching process generates this event. It is also seen that the power law with a slope of 3 envelopes the data for the highest amplitudes of  $\omega_z^2$  from below. Further details cannot be provided on the basis of the measurements due to the missing velocity derivatives. Note also that the analysis is conducted locally in contrast to (13).

**C. Reservoir computing model for dynamical evolution of vorticity**

Finally, we apply a reservoir computing model (RCM) to reconstruct the spatial structure of  $\omega_z$  in the measurement region  $A$ . The corresponding procedure is visualized in Fig. 2(b) and follows that of Lu *et al.* [32] taken to reconstruct the dynamics of the one-dimensional Kuramoto-Sivashinsky

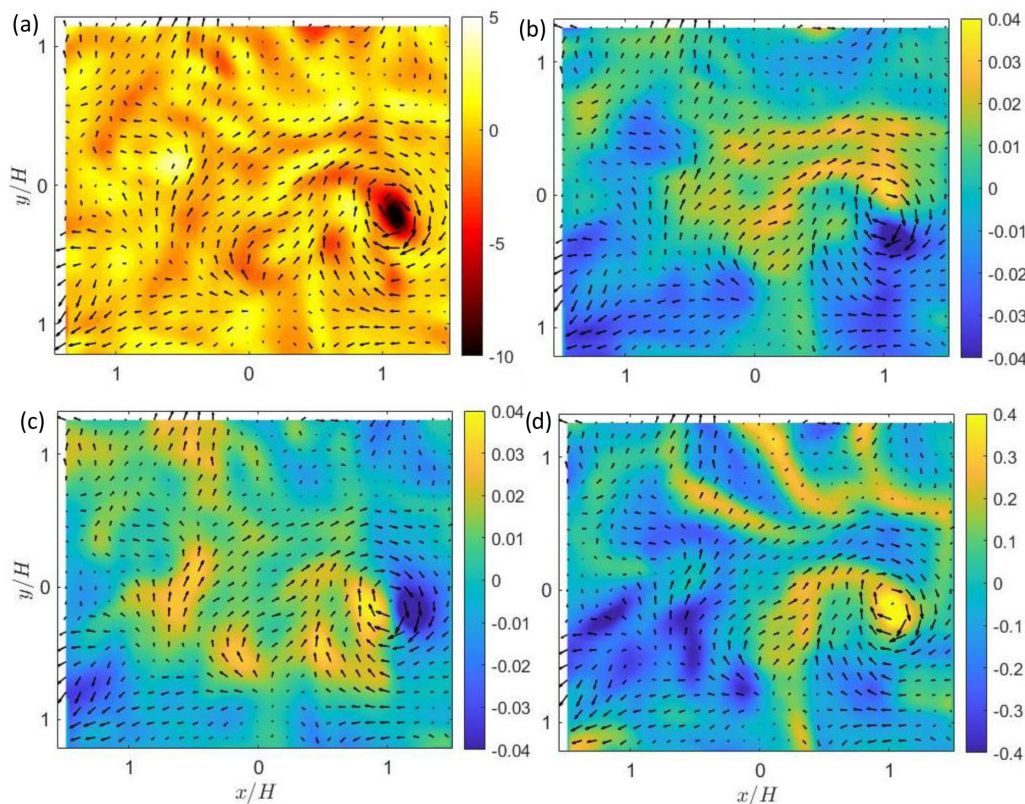


FIG. 6. Visualization of an extreme event of  $\omega_z$  from the SPIV measurements at  $Ra = 5.1 \times 10^5$ . Filled contours of  $\omega_z$  in (a),  $u_x$  in (b),  $u_y$  in (c), and  $u_z$  in (d) are shown. Color bars of the vorticity and velocity components are given in units of  $t_{fr}$  and  $U_{fr}$ , respectively. Arrows show the same in-plane velocity vector field in all four panels.

equation. We therefore provide time series of the measurements sampled on a very coarse uniform grid that covers the measurement region  $A$  as seen in the sketch. The RCM is then trained to generate time series of the vorticity component at the remaining and surrounding grid points of the measurement region  $A$ . The procedure allows us to reconstruct the space-time dynamics of the vorticity component in  $A$ .

In Table III, we summarize the optimal hyperparameters of the RCM that are chosen after the training procedure for the time-series prediction. All time series consist of  $10^4$  PIV snapshots. The first  $N_T = 5000$  snapshots were used to train the RCM model,  $N_V = 1000$  for validation, and the remaining  $N_P = 4000$  data snapshots are unseen test data in the reconstruction phase. Furthermore, we list the mean-squared errors (MSE) in the table, which follow for the training ( $T$ ), validation ( $V$ ), and reconstruction ( $R$ ) phases. These errors are given by

$$\text{MSE}_{\xi} = \frac{1}{N_{\xi}} \sum_{n=1}^{N_{\xi}} \frac{1}{N_{\text{PIV}}} \sum_{k=1}^{N_{\text{PIV}}} [\Omega_k(n) - \hat{\Omega}_k^{\text{out}}(n)]^2, \quad (14)$$

where  $\Omega(n)$  is again the ground truth and  $\hat{\Omega}^{\text{out}}(n)$  is the RCM output. Here,  $\xi = \{T, V, R\}$ . In the reconstruction phase, the seed and hyperparameter set is used that gave the lowest MSE together with a sufficiently low Kullback-Leibler divergence [29], which is a second measure that was taken and defined as

$$\text{KL}(p, q) = \sum_{\omega_z} p(\omega_z) \log_e \frac{p(\omega_z)}{q(\omega_z)}, \quad (15)$$

where  $p$  and  $q$  are the PDFs obtained from ground truth and RCM output in the validation phase, respectively. Note that  $\text{KL} = 0$  if  $p = q$  for the PDFs. We run such a hyperparameter tuning for all six convection data records. The best RCM for each Rayleigh number is then used for the reconstruction task.

TABLE III. Summary of the optimal hyperparameters. Here, each run was trained individually. Furthermore, the mean-squared error (MSE) of the training ( $T$ ), validation ( $V$ ), and reconstruction ( $R$ ) phases is given. The optimal parameters were chosen for  $N \in [1000, 3000]$ ,  $\rho(W_r) \in [0.9, 1]$ ,  $\gamma \in [0.01, 1]$ , and  $\alpha \in [0.1, 1]$ . For each of 10 different random configurations of the reservoir matrix  $W^r$ , 100 different random combinations of the hyperparameters within the given intervals were taken. The last row displays the Kullback-Leibler divergence in the reconstruction phase.

	Ra = $1.7 \times 10^4$			Ra = $2.9 \times 10^5$		
	3 × 3	5 × 5	7 × 7	3 × 3	5 × 5	7 × 7
$N$	2523	2721	2687	2741	2299	2885
$\alpha$	0.74	0.14	0.39	0.33	0.22	0.57
$\rho(W^r)$	0.94	0.98	0.98	0.95	0.92	0.93
$\gamma$	0.58	0.54	0.88	0.18	0.02	0.64
$D$	0.2	0.2	0.2	0.2	0.2	0.2
$\text{MSE}_T$	0.029	0.024	0.047	0.098	0.208	0.29
$\text{MSE}_V$	0.039	0.18	0.27	0.27	0.49	0.79
$\text{MSE}_R$	0.041	0.181	0.281	0.24	0.44	0.72
KL	0.005	0.006	0.014	0.001	0.001	0.003



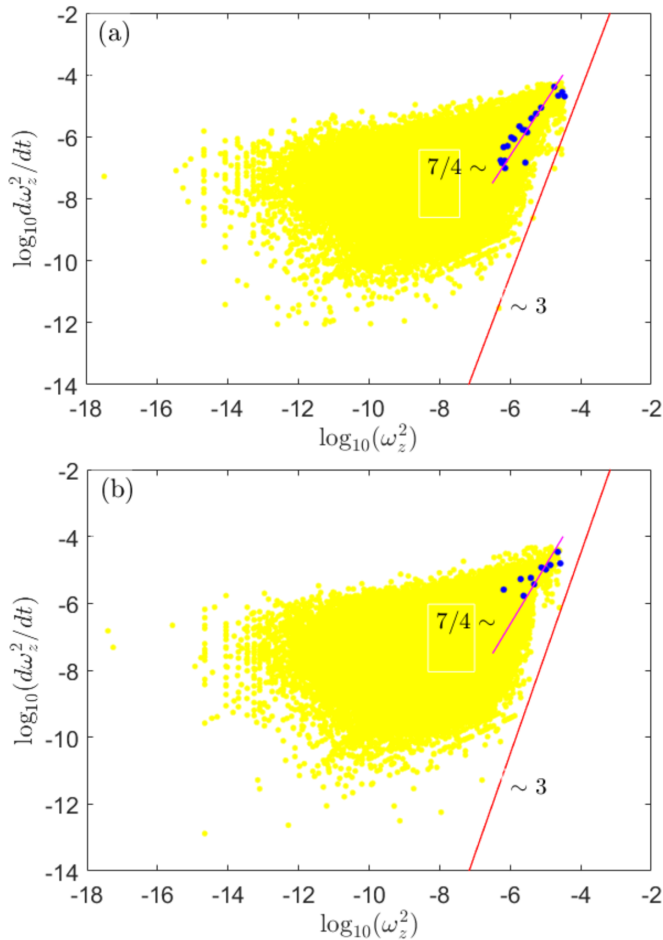


FIG. 7. Scatter plots of the time series, taken at the 25 grid points around extreme event position  $\mathbf{x}_*$  for  $Ra = 5.1 \times 10^5$ . Panels (a) and (b) represent the two events at  $t = 853.25t_{ff}$  and  $599t_{ff}$ , respectively, for which  $|\omega_z| \geq 10\omega_{z,rms}$ . The squared out-of-plane vorticity growth is plotted vs the squared out-of-plane vorticity. The final data points with  $t < t_*$  are replotted in blue. Also indicated are the scaling exponents that follow from [53].

Three different scenarios, namely learning the vorticity time series on  $3 \times 3$ ,  $5 \times 5$ , and  $7 \times 7$  grid points around continually provided data points, have been investigated. These three scenarios correspond to providing 11%, 3.5%, and 1.9% of the total number of grid points, respectively. We have conducted this analysis for the smallest and one of the largest Rayleigh numbers of our data record,  $Ra = 1.7 \times 10^4$  and  $2.9 \times 10^5$ . The results are summarized correspondingly in Figs. 8 and 9. Panels (a) and (b) in both figures display the reconstruction of an example of a time series taken at a specific position in  $A$ . We see that in both cases, the time dependence is approximated fairly well by the reservoir computing model. Both figures are obtained for a  $5 \times 5$  reconstruction scenario. Panel (b) magnifies the initial time steps  $n$  of the reconstruction phase. Panels (c) and (d) of both figures display the PDFs that result for the normalized vorticity component from the RCM in comparison to the experimental test data. While the velocity derivative statistics for the smallest Rayleigh number is still very close to a Gaussian distribution, it has crossed over to the non-Gaussian intermittent regime for the higher

Rayleigh number. This becomes visible by the extended tails that are also reproduced well by our machine-learning algorithm. The PDFs in both panels are shown for two scenarios,  $3 \times 3$  and  $7 \times 7$ , in each case. Note that the latter scenario implies that less information about the input is provided for the machine-learning algorithm during the prediction phase. Only every 49th grid point contains a partial observation. We can see again that the statistics in both cases are in fair agreement with the experimental results. The RCM with continually available sparse data is thus able to reconstruct the statistical properties of a highly intermittent out-of-plane vorticity component. In Fig. 10, we demonstrate the capability of the trained recurrent neural network to reconstruct an extreme vorticity event. A typical event, which is detected at a time  $t = t_*$  (that translates into snapshot number  $n = n_*$ ), is shown here. We therefore compare a sequence of PIV snapshots with the corresponding model predictions. The RCM results have been composed of  $3 \times 3$  reconstructions. The panels have been subsequently smoothed by a  $6 \times 6$  procedure averaging. It can be seen that the figures at the corresponding times agree well with each other. We can thus conclude from this visual inspection that extreme or high-amplitude vorticity events can be reconstructed by the specific recurrent machine-learning algorithm.

In Fig. 11, the squared out-of-plane vorticity or out-of-plane enstrophy  $E(t)$  is integrated over the observation plane  $A$ . The quantity is given by

$$E(t) := \int_A \frac{\omega_z^2(t)}{2} dA \quad (16)$$

and displayed for two Rayleigh numbers. The snapshot number of the global vorticity component maximum is denoted as  $n_*$ . The quantitative comparison of the three predictions with the experimental test data demonstrates that all three scenarios follow the ground truth data fairly well. As expected, the deviations increase with increasing spatial sparsity of the available partial observations. This is very well visible for the larger of the two Rayleigh numbers. For the more quantitative analysis, we refer also to  $MSE_R$  in Table III.

The ability of generalization of the RCM is shown in Fig. 12. Two RCMs, one for the  $3 \times 3$  scenario and one for the  $7 \times 7$  scenario, are trained and validated on the data with the lowest available Rayleigh number  $Ra = 1.7 \times 10^4$  and then tested on unseen data at  $Ra = 1.1 \times 10^5$  and  $2.9 \times 10^5$ . The figure shows a representative comparison between the reconstructed time series on a selected PIV grid point and its corresponding ground truth. The reconstructed time series follow the ground truth very well for all scenarios, which shows that the RCM can generalize over a certain range of experimental conditions including higher levels of turbulence.

We finally note here that for a reconstruction without partial observations, i.e., for a fully autonomous RCM prediction (also known as the closed-loop scenario), the time series at the grid points of the measurement section  $A$  start to deviate after a few time steps  $n$  for the highest Rayleigh numbers of our data record. This deviation is a known problem of RCMs [33]. It can be mitigated by using other recurrent neural network architectures such as long short-term memory networks or gated recurrent units trained with backpropagation [33,34,54].

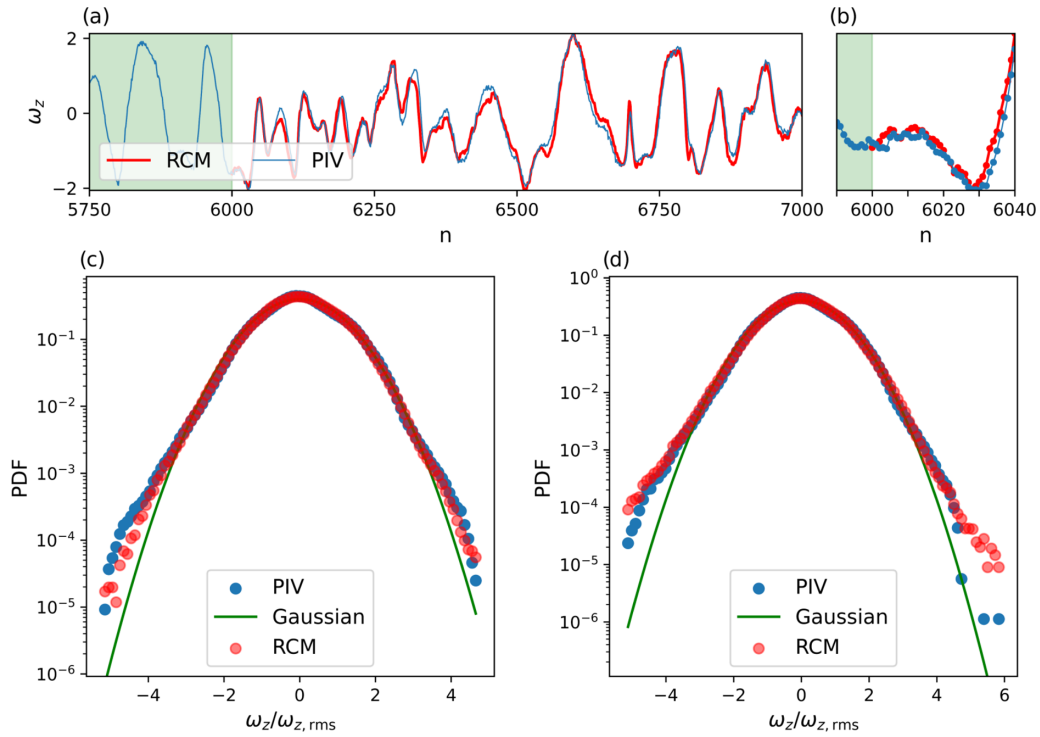


FIG. 8. Reconstruction of temporal evolution and statistics of the out-of-plane vorticity component  $\omega_z$  by reservoir computing models. The Rayleigh number is  $Ra = 1.7 \times 10^4$ . (a) Time-series reconstruction example at one grid point in *A*. Integer  $n$  corresponds to time  $n\Delta t$  with  $\Delta t = 0.25t_{ff}$ . The green shaded area indicates the validation phase. (b) Zoom into the first steps of the reconstruction phase. Panel (c) shows the probability density function obtained from a reconstruction of correspondingly eight grid points around each continually available data point (scenario  $3 \times 3$ ) and panel (d) from 48 grid points (scenario  $7 \times 7$ ).

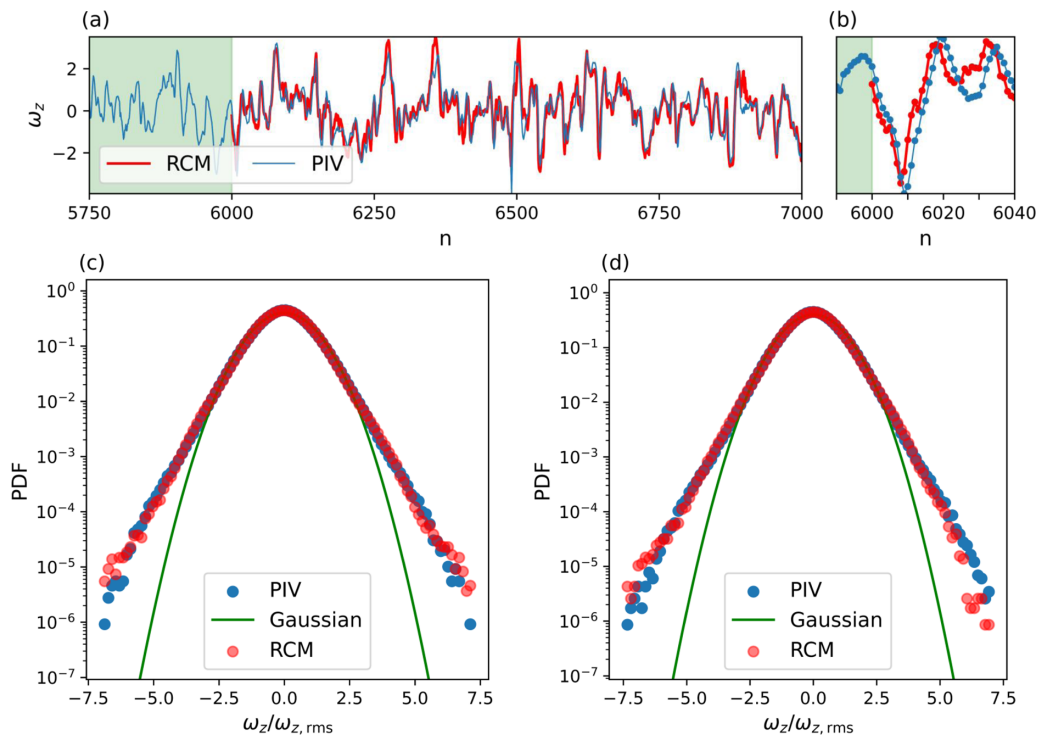


FIG. 9. Same as in Fig. 8 for  $Ra = 2.9 \times 10^5$  with  $\Delta t = 0.25t_{ff}$ .

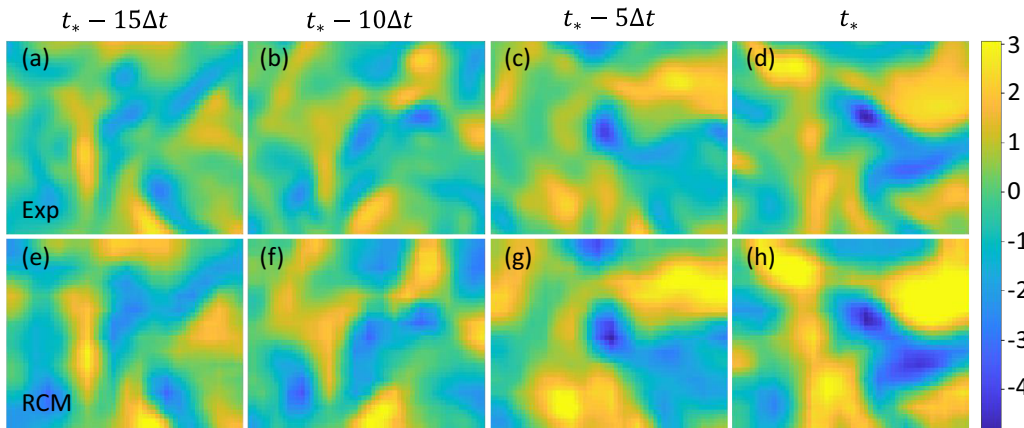


FIG. 10. Dynamical sequence of an extreme vorticity event (a)–(d) and its reconstruction by the reservoir computing model algorithm with the  $3 \times 3$  scenario (e)–(h). The extreme event of  $\omega_z$  is at time  $t = t_*$ . The time interval between two snapshots is  $\Delta t = 0.25t_{ff}$ . The Rayleigh number is  $Ra = 2.9 \times 10^5$ .

IV. SUMMARY AND OUTLOOK

Our present work was motivated by two major scientific objectives: (i) a detailed analysis of the intermittent statistics of velocity derivatives in the bulk of a turbulent Rayleigh-Bénard convection flow in air by means of stereoscopic particle image velocimetry measurement, including the monitoring of high-amplitude events of the out-of-plane vorticity component, and (ii) the machine-learning-assisted reconstruction of the dynamical evolution and statistics of small-scale velocity derivatives, including the reconstruction of extreme or high-amplitude events. Therefore, the moderate Rayleigh numbers were varied over an order of magnitude, in a range for which the statistics of the spatial velocity derivatives (and

thus of the vorticity components) goes over from Gaussian to non-Gaussian, as discussed in our recent direct numerical simulations [23]. This transition in the derivative statistics was detected by both the experiments and the subsequent machine-learning algorithm, which is based on a recurrent neural network in the form of a reservoir computing model. The latter was trained on the experimental PIV data.

As in most laboratory experiments, and in contrast to direct numerical simulations, the three velocity components of the turbulent convection flow were detectable in a horizontal section only and not fully resolved in the whole volume. Exceptions are high-resolution experiments, which are practically almost as expensive in their postprocessing as fully resolved direct numerical simulations [55,56]. SPIV allows us to reconstruct seven out of the nine components of the velocity gradient tensor  $M_{ij}$  together with the out-of-plane vorticity component  $\omega_z$ . In many situations, such as field measurements, the time series data are taken at sparsely distributed locations. These practical constraints suggest the application of (recurrent) machine-learning algorithms. They can process sequential data, make predictions on the dynamics, and thus add missing dynamical information on the turbulence fields. In the second part of this work, we had exactly such a proof-of-concept in mind when investigating the reconstruction capabilities of the applied reservoir computing model, particularly those of extreme or high-amplitude vorticity events.

The studies can be extended in several directions. One direction would be a combination with temperature measurements close to the boundary layer, such that strong plume detachments can serve as precursors for extreme dissipation or vorticity events in the bulk of the convection layer. This idea has been developed in Ref. [23] on the basis of fully resolved DNS. In this case, superresolution generative adversarial networks can reconstruct the temperature field from coarse measurements close to the wall. A similar path has been taken for near-wall velocity measurements in Ref. [57]. A further direction consists of the design of generative algorithms that produce time series of the missing two velocity derivative components complemented by the existing statistical symmetries in the flow at hand [58,59]. In this way,

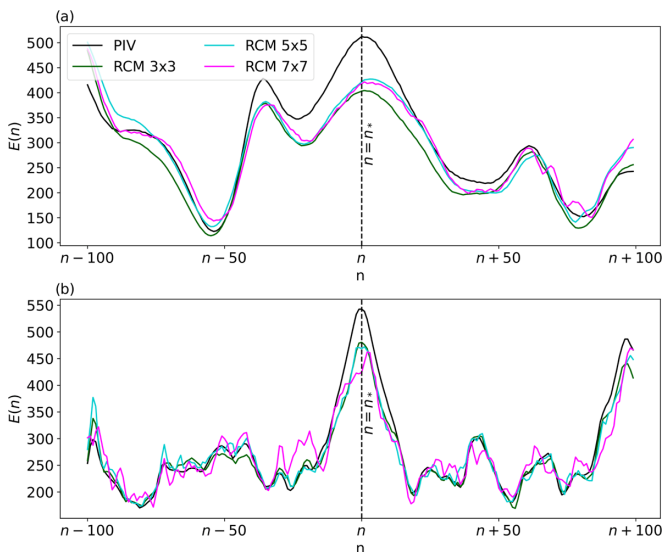


FIG. 11. Time series of the out-of-plane enstrophy  $E(n)$  for two Rayleigh numbers, (a)  $Ra = 1.7 \times 10^4$  and (b)  $Ra = 2.9 \times 10^5$ , which is calculated by Eq. (16). Both plots compare the measurement data with the reservoir computing reconstructions, which have been obtained either by the  $3 \times 3$ , the  $5 \times 5$ , or the  $7 \times 7$  scenario as indicated in the legend of panel (a). Note that argument  $n$  stands for time  $t = n\Delta t$ .

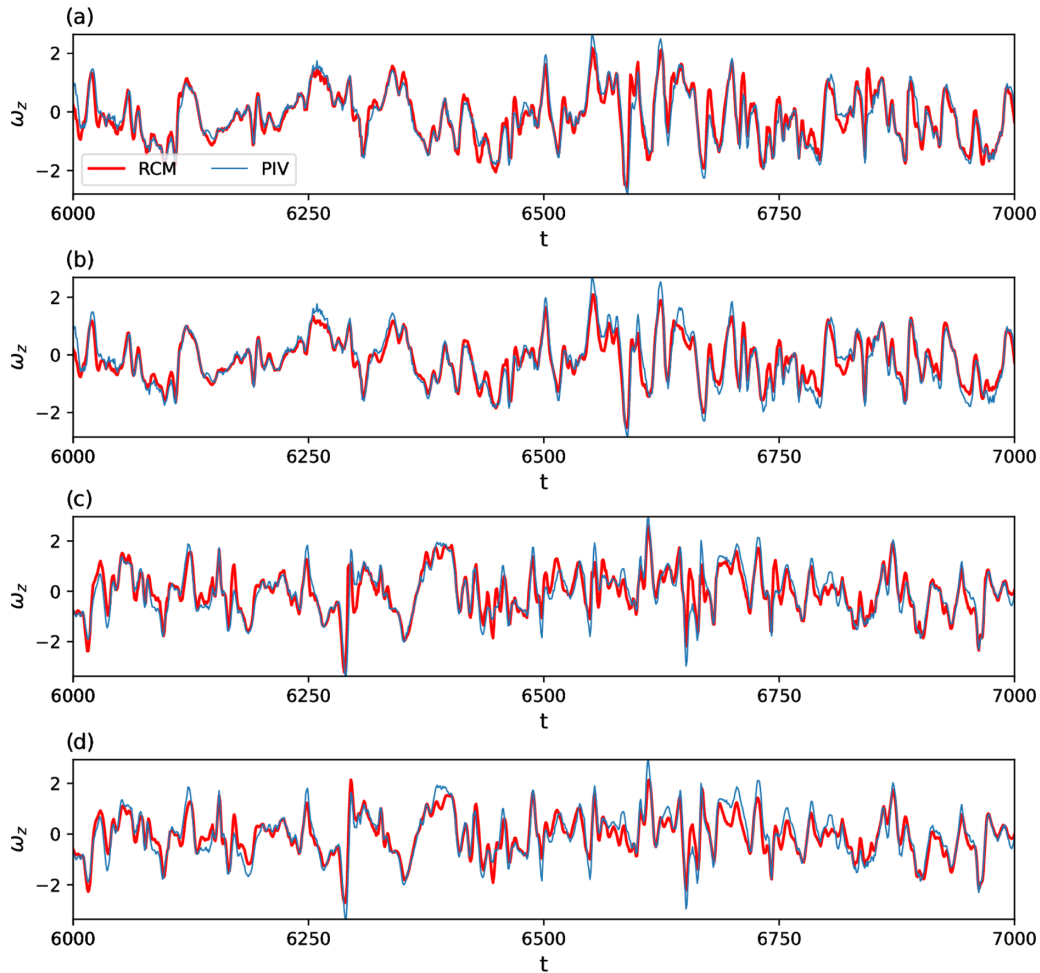


FIG. 12. Generalization capability of the reservoir computing model. We show examples of reconstructed time series at one grid point in  $A$ . Integer  $n$  corresponds to time  $n\Delta t$  with  $\Delta t = 0.25t_{ff}$ . Two RCMs were trained at  $Ra = 1.7 \times 10^4$  and used for the reconstruction task for unseen data at  $Ra = 1.1 \times 10^5$  (a),(b) and  $Ra = 2.9 \times 10^5$  (c),(d). The first panel for each Rayleigh number shows the  $3 \times 3$  scenario of reconstruction (a),(c) and the second panel shows the  $7 \times 7$  scenario (b),(d).

machine-learning-assisted measurements of the kinetic energy and thermal dissipation rates would be possible without the usage of tomographic techniques. Studies in this direction are currently underway and will be reported elsewhere.

#### ACKNOWLEDGMENTS

The authors would like to thank Alexander Thieme for the support with the experiments, and Florian Heyder for helpful

remarks. The work of V.V. was partly supported by Priority Programme DFG-SPP 1881 on Turbulent Superstructures of the Deutsche Forschungsgemeinschaft (DFG). Her work is currently supported by the Marie Skłodowska-Curie Fellowship of the European Union with Project No. 101024531. The work of R.K. is supported by project SCHU 1410/30-1 of the DFG. Training and prediction of the machine learning algorithm were carried out on up to 8 CPUs of the compute cluster Makalu at Technische Universität Ilmenau.

- 
- [1] L. P. Kadanoff, Turbulent heat flow: Structures and scaling, *Phys. Today* **54**(8), 34 (2001).
  - [2] G. Ahlers, S. Grossmann, and D. Lohse, Heat transfer and large scale dynamics in turbulent Rayleigh-Bénard convection, *Rev. Mod. Phys.* **81**, 503 (2009).
  - [3] F. Chillà and J. Schumacher, New perspectives in turbulent Rayleigh-Bénard convection, *Eur. Phys. J. E* **35**, 58 (2012).
  - [4] M. K. Verma, *Physics of Buoyant Flows* (World Scientific, Singapore, 2018).
  - [5] T. Hartlep, A. Tilgner, and F. H. Busse, Large Scale Structures in Rayleigh-Bénard Convection at High Rayleigh Numbers, *Phys. Rev. Lett.* **91**, 064501 (2003).
  - [6] A. Parodi, J. von Hardenberg, G. Passoni, A. Provenzale, and E. A. Spiegel, Clustering of Plumes in Turbulent Convection, *Phys. Rev. Lett.* **92**, 194503 (2004).
  - [7] T. Hartlep, A. Tilgner, and F. H. Busse, Transition to turbulent convection in a fluid layer heated from below at moderate aspect ratio, *J. Fluid Mech.* **544**, 309 (2005).

- [8] J. von Hardenberg, A. Parodi, G. Passoni, A. Provenzale, and E. A. Spiegel, Large-scale patterns in Rayleigh-Bénard convection, *Phys. Lett. A* **372**, 2223 (2008).
- [9] J. Bailon-Cuba, M. S. Emran, and J. Schumacher, Aspect ratio dependence of heat transfer and large-scale flow in turbulent convection, *J. Fluid Mech.* **655**, 152 (2010).
- [10] M. S. Emran and J. Schumacher, Large-scale mean patterns in turbulent convection, *J. Fluid Mech.* **776**, 96 (2015).
- [11] A. Pandey, J. D. Scheel, and J. Schumacher, Turbulent Superstructures in Rayleigh-Bénard convection, *Nat. Commun.* **9**, 2118 (2018).
- [12] R. J. A. M. Stevens, A. Blass, X. Zhu, R. Verzicco, and D. Lohse, Turbulent thermal superstructures in Rayleigh-Bénard convection, *Phys. Rev. Fluids* **3**, 041501 (2018).
- [13] E. Fonda, A. Pandey, J. Schumacher, and K. R. Sreenivasan, Deep learning in turbulent convection networks, *Proc. Natl. Acad. Sci. USA* **116**, 8667 (2019).
- [14] V. Valori, A. Innocenti, B. Dubrulle, and S. Chibbaro, Weak formulation and scaling properties of energy fluxes in three-dimensional numerical turbulent Rayleigh-Bénard convection, *J. Fluid Mech.* **885**, A14 (2019).
- [15] G. Green, D. G. Vlaykov, J. P. Mellado, and M. Wilczek, Resolved energy budget of superstructures in Rayleigh-Bénard convection, *J. Fluid Mech.* **887**, A21 (2020).
- [16] D. Krug, D. Lohse, and R. J. A. M. Stevens, Coherence of temperature and velocity superstructures in turbulent Rayleigh-Bénard flow, *J. Fluid Mech.* **887**, A2 (2020).
- [17] P. Berghout, W. J. Baars, and D. Krug, The large-scale footprint in small-scale Rayleigh-Bénard turbulence, *J. Fluid Mech.* **911**, A62 (2021).
- [18] J. W. Deardorff and G. E. Willis, Investigation of turbulent thermal convection between horizontal plates, *J. Fluid Mech.* **28**, 675 (1967).
- [19] D. E. Fitzjarrald, An experimental study of turbulent convection in air, *J. Fluid Mech.* **73**, 693 (1976).
- [20] D. Schmeling, J. Bosbach, and C. Wagner, Simultaneous measurement of temperature and velocity fields in convective air flows, *Meas. Sci. Technol.* **25**, 035302 (2014).
- [21] C. Kästner, C. Resagk, J. Westphalen, M. Junghähnel, C. Cierpka, and J. Schumacher, Assessment of horizontal velocity fields in square thermal convection cells with large aspect ratio, *Exp. Fluids* **59**, 171 (2018).
- [22] C. Cierpka, C. Kästner, C. Resagk, and J. Schumacher, On the challenges for reliable measurements of convection in large aspect ratio Rayleigh-Bénard cells in air and sulfur-hexafluoride, *Exp. Therm. Fluid Sci.* **109**, 109841 (2019).
- [23] V. Valori and J. Schumacher, Connecting boundary layer dynamics with extreme bulk dissipation events in Rayleigh-Bénard flow, *Europhys. Lett.* **134**, 34004 (2021).
- [24] J. Schumacher, B. Eckhardt, and C. R. Doering, Extreme vorticity growth in Navier-Stokes turbulence, *Phys. Lett. A* **374**, 861 (2010).
- [25] J. D. Scheel, M. S. Emran, and J. Schumacher, Resolving the fine-scale structure in turbulent Rayleigh-Bénard convection, *New J. Phys.* **15**, 113063 (2013).
- [26] P. K. Yeung, X. M. Zhai, and K. R. Sreenivasan, Extreme events in computational turbulence, *Proc. Natl. Acad. Sci. USA* **112**, 12633 (2015).
- [27] D. Buaria, A. Pumir, and E. Bodenschatz, Self-attenuation of extreme events in Navier-Stokes turbulence, *Nat. Commun.* **11**, 5852 (2020).
- [28] J. Schumacher and J. D. Scheel, Extreme dissipation event due to plume collision in a turbulent convection cell, *Phys. Rev. E* **94**, 043104 (2016).
- [29] I. Goodfellow, Y. Bengio, and A. Courville, *Deep Learning* (MIT Press, Cambridge, MA, 2016).
- [30] H. Jaeger and H. Haas, Harnessing nonlinearity: Predicting chaotic systems and saving energy in wireless communication, *Science* **304**, 78 (2004).
- [31] S. Pandey, J. Schumacher, and K. R. Sreenivasan, A perspective on machine learning in turbulent flows, *J. Turbul.* **21**, 567 (2020).
- [32] Z. Lu, J. Pathak, B. R. Hunt, M. Girvan, R. Brockett, and E. Ott, Reservoir observers: Model-free inference of unmeasured variables in chaotic systems, *Chaos* **27**, 041102 (2017).
- [33] P. R. Vlachas, J. Pathak, B. R. Hunt, T. P. Sapsis, M. Girvan, E. Ott, and P. Koumoutsakos, Backpropagation algorithms and reservoir computing in recurrent neural networks for the forecasting of complex spatiotemporal dynamics, *Neural Netw.* **126**, 191 (2020).
- [34] P. R. Vlachas, G. Arampatzis, C. Uhler, and P. Koumoutsakos, Multiscale simulations of complex systems by learning their effective dynamics, *Nat. Mach. Intell.* **4**, 359 (2022).
- [35] P. A. Srinivasan, L. Guastoni, H. Azizpour, P. Schlatter, and R. Vinuesa, Predictions of turbulent shear flows using deep neural networks, *Phys. Rev. Fluids* **4**, 054603 (2019).
- [36] H. Eivazi, L. Guastoni, P. Schlatter, H. Azizpour, and R. Vinuesa, Recurrent neural networks and Koopman-based frameworks for temporal predictions in a low-order model of turbulence, *Int. J. Heat Fluid Flow* **90**, 108816 (2021).
- [37] A. Asch, E. Brady, H. Gallardo, J. Hood, B. Chu, and M. Farazmand, Model-assisted deep learning of rare extreme events from partial observations, *Chaos* **32**, 043112 (2022).
- [38] S. Pandey and J. Schumacher, Reservoir computing model of two-dimensional turbulent convection, *Phys. Rev. Fluids* **5**, 113506 (2020).
- [39] F. Heyder and J. Schumacher, Echo state network for two-dimensional moist Rayleigh-Bénard convection, *Phys. Rev. E* **103**, 053107 (2021).
- [40] T. P. Sapsis, Statistics of extreme events in fluid flows and waves, *Annu. Rev. Fluid Mech.* **53**, 85 (2021).
- [41] B. Wieneke, Stereo-PIV using self-calibration on particle images, *Exp. Fluids* **39**, 267 (2005).
- [42] V. Valori, Doctoral thesis, Delft University of Technology (2018).
- [43] V. Valori, G. E. Elsinga, M. Rohde, J. Westerweel, and T. H. J. van der Hagen, Particle image velocimetry measurements of a thermally convective supercritical fluid, *Exp. Fluids* **60**, 143 (2019).
- [44] V. Valentina, A. Thieme, C. Cierpka, and J. Schumacher, Rayleigh-Bénard convection in air: Out-of-plane vorticity from stereoscopic PIV measurements, in *Proceedings of the 14th International Symposium on Particle Image Velocimetry* (Illinois Institute of Technology, Chicago, USA, 2021), Vol. 1, p. 2018.
- [45] R. J. Adrian and J. Westerweel, *Particle Image Velocimetry* (Cambridge University Press, Cambridge, UK, 2011).

- [46] M. Raffel, C. E. Willert, F. Scarano, C. J. Kähler, S. T. Wereley, and J. Kompenhans, *Particle Image Velocimetry: A Practical Guide* (Springer, Berlin, 2018).
- [47] E. W. Lemmon, M. L. Huber, and M. O. McLinden, NIST standard reference database 23: Reference fluid thermodynamic and transport properties—REFPROP, Version 9.1. Standard Reference Data Program, National Institute of Standards and Technology, 2013.
- [48] G. E. Elsinga, B. W. Van Oudheusden, and F. Scarano, Evaluation of aero-optical distortion effects in PIV, *Exp. Fluids* **39**, 246 (2005).
- [49] B. Wieneke, PIV uncertainty quantification from correlation statistics, *Meas. Sci. Technol.* **26**, 074002 (2015).
- [50] M. Lukoševičius and A. Uselis, Efficient implementations of echo state network cross-validation, *Cogn. Comput.* (2021).
- [51] J. Schumacher, J. D. Scheel, D. Krasnov, D. A. Donzis, V. Yakhot, and K. R. Sreenivasan, Small-scale universality in fluid turbulence, *Proc. Natl. Acad. Sci. USA* **111**, 10961 (2014).
- [52] J. Schumacher, A. Pandey, V. Yakhot, and K. R. Sreenivasan, Transition to turbulence scaling in Rayleigh-Bénard convection, *Phys. Rev. E* **98**, 033120 (2018).
- [53] L. Lu and C. R. Doering, Limits on enstrophy growth for solutions of 3D Navier-Stokes equations, *Ind. Univ. Math. J.* **57**, 2693 (2008).
- [54] S. Pandey, P. Teutsch, P. Mäder, and J. Schumacher, Direct data-driven forecast of local turbulent heat flux in Rayleigh-Bénard convection, *Phys. Fluids* **34**, 045106 (2022).
- [55] J. Westerweel, G. E. Elsinga, and R. J. Adrian, Particle image velocimetry for complex and turbulent flows, *Annu. Rev. Fluid Mech.* **45**, 409 (2013).
- [56] D. Schanz, S. Gesemann, and A. Schröder, Shake-The-Box: Lagrangian particle tracking at high image densities, *Exp. Fluids* **57**, 70 (2016).
- [57] A. Güemes, S. Discetti, A. Ianiro, B. Sirmacek, H. Azizpour, and R. Vinuesa, From coarse wall measurements to turbulent velocity fields through deep learning, *Phys. Fluids* **33**, 075121 (2021).
- [58] M. Mattheakis, P. Protopapas, D. Sondak, M. Di Giovanni, and E. Kaxiras, Physical symmetries embedded in neural networks, [arXiv:1904.08991](https://arxiv.org/abs/1904.08991).
- [59] G. E. Karniadakis, I. G. Kevrekidis, L. Lu, P. Perdikaris, S. Wang, and L. Yang, Physics-informed machine learning, *Nat. Rev. Phys.* **3**, 422 (2021).